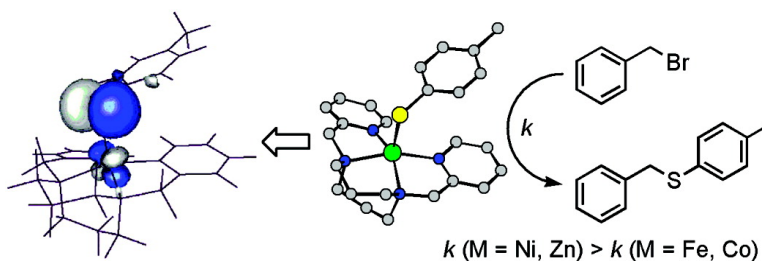Article

Electronic Structure Control of the Nucleophilicity of Transition Metal−Thiolate Complexes: An Experimental and Theoretical Study

Derek C. Fox, Adam T. Fiedler, Heather L. Halfen, Thomas C. Brunold, and Jason A. Halfen

k (M = Ni, Zn) > k (M = Fe, Co)

More About This Article

Additional resources and features associated with this article are available within the HTML version:

- Supporting Information
- Links to the 7 articles that cite this article, as of the time of this article download
- Access to high resolution figures
- Links to articles and content related to this article
- Copyright permission to reproduce figures and/or text from this article

View the Full Text HTML

Electronic Structure Control of the Nucleophilicity of Transition Metal−Thiolate Complexes: An Experimental and Theoretical Study

Derek C. Fox,[†] Adam T. Fiedler,[‡] Heather L. Halfen,[†] Thomas C. Brunold,*,[‡] and Jason A. Halfen*,[†]

Contribution from the Department of Chemistry, University of Wisconsin-Madison, 1101 West University Avenue, Madison, Wisconsin 53706, and Department of Chemistry, University of Wisconsin-Eau Claire, 105 Garfield Avenue, Eau Claire, Wisconsin 54702

Received November 4, 2003; E-mail: brunold@chem.wisc.edu; halfenja@uwec.edu

Abstract: New metal(II)−thiolate complexes supported by the tetradentate ligand 1,5-bis(2-pyridylmethyl)-1,5-diazacyclooctane (L^8py_2) have been synthesized and subjected to physical, spectroscopic, structural, and computational characterization. The X-ray crystal structures of these complexes, $[L^8py_2M(S\text{-}C_6H_4\text{-}p\text{-}CH_3)]BPh_4$ (M = Co, Ni, Zn), reveal distorted square-pyramidal divalent metal ions with four equatorial nitrogen donors from L^8py_2 and axial *p*-toluenethiolate ligands. The reactions of the complexes with benzyl bromide produce isolable metal(II)−bromide complexes (in the cases of Co and Ni) and the thioether benzyl-*p*-tolylsulfide. This reaction is characterized by a second-order rate law ($v = k_2[L^8py_2M(SAr)^+][PhCH_2Br]$) for all complexes (where M = Fe, Co, Ni, or Zn). Of particular significance is the disparity between k_2 for M = Fe and Co versus k_2 for M = Ni and Zn, in that k_2 for M = Ni and Zn is ca. 10 times larger (faster) than k_2 for M = Fe and Co. An Eyring analysis of k_2 for $[L^8py_2Co(SAr)]^+$ and $[L^8py_2Ni(SAr)]^+$ reveals that the reaction rate differences are not rooted in a change in mechanism, as the reactions of these complexes with benzyl bromide exhibit comparable activation parameters (M = Co: $\Delta H^\ddagger = 45(2)$ kJ mol^{-1}, $\Delta S^\ddagger = -144(6)$ J mol^{-1} K^{-1}; M = Ni: $\Delta H^\ddagger = 43(3)$ kJ mol^{-1}, $\Delta S^\ddagger = -134(8)$ J mol^{-1} K^{-1}). Electronic structure calculations using density functional theory (DFT) reveal that the enhanced reaction rate for $[L^8py_2Ni(SAr)]^+$ is rooted in a four-electron repulsion (or a "filled/filled interaction") between a completely filled nickel-(II) d_π orbital and one of the two thiolate frontier orbitals, a condition that is absent in the Fe(II) and Co(II) complexes. The comparable reactivity of $[L^8py_2Zn(SAr)]^+$ relative to that of $[L^8py_2Ni(SAr)]^+$ arises from a highly ionic zinc(II)−thiolate bond that enhances the negative charge density on the thiolate sulfur. DFT calculations on putative thioether-coordinated intermediates reveal that the Co(II)− and Zn(II)−thioethers exhibit weaker M−S bonding than Ni(II). These combined results suggest that while Ni(II) may serve as a competent replacement for Zn(II) in alkyl group transfer enzymes, turnover may be limited by slow product release from the Ni(II) center.

Introduction

Alkyl group transfer to a metal-bound cysteine thiolate is a significant reaction in metallobiochemistry and is mediated by a number of zinc-containing enzymes.[1] For example, the Ada protein, which contains a Cys_4Zn active site, participates in the repair of DNA that has been methylated along its phosphate ester backbone by transfer of a methyl group to a zinc-bound cysteinate ligand.[2] The methionine synthases MetE and MetH catalyze the formation of the amino acid methionine by alkyl group transfer from either methyltetrahydrofolate (MetE) or methylcobalamin (MetH) to a zinc-bound homocysteinate ligand.[3] Farnesyl protein transferases (FPTs) are responsible for the post-translational isoprenylation of cysteine-terminal proteins and function through coordination of the target protein's terminal

cysteine residue to the FPT active-site zinc ion.[4] This zinc-mediated modification is required to generate proteins that are implicated in tumor development (Ras proteins) and makes FPTs attractive targets for anti-cancer therapeutic agents.[5] Underpinning the function of this diverse group of metalloproteins is the nucleophilic reactivity of a zinc−thiolate unit, and the biological significance of these reactions provides substantial impetus for delineating the factors that govern the nucleophilicity of transition metal−thiolate complexes.

Fundamental investigations of the alkylation reactivity of synthetic metal−thiolate complexes have provided insight into the nucleophilic character of such species. Lippard and co-

† University of Wisconsin-Eau Claire.
‡ University of Wisconsin-Madison.

(1) Matthews, R. G.; Goulding, C. W. *Curr. Opin. Chem. Biol.* **1997**, 332−339.
(2) Myers, L. C.; Terranova, M. P.; Ferentz, A. E.; Wagner, G.; Verdine, G. L. *Science* **1993**, *261*, 1165−1167.

(3) (a) Whitfield, C. D.; Steers, E. J., Jr.; Weisbach, H. *J. Biol. Chem.* **1970**, *245*, 390−401. (b) Gonzalez, J. C.; Banerjee, R. V.; Huang, S.; Sumner, J. S.; Matthews, R. G. *Biochemistry* **1992**, *31*, 6045−6056. (c) Peariso, K.; Zhou, Z. S.; Smith, A. E.; Matthews, R. G.; Penner-Hahn, J. E. *Biochemistry* **2001**, *40*, 987−993.
(4) (a) Hightower, K. E.; Fierke, C. A. *Curr. Opin. Chem. Biol.* **1999**, *3*, 176−181. (b) Tobin, D. A.; Pickett, J. S.; Hartman, H. L.; Fierke, C. A.; Penner-Hahn, J. E. *J. Am. Chem. Soc.* **2003**, *125*, 9962−9969.
(5) (a) Gibbs, J. B. *Cell* **1991**, *65*, 1−4. (b) Leonard, D. M. *J. Med. Chem.* **1997**, *40*, 2971−2990.

M		
Fe	**1**
Co	**2**
Ni	**3**
Zn	**4**
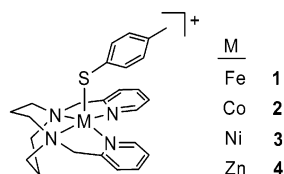
workers studied the reactions of anionic tetrathiolate complexes of zinc(II) and mercury(II) with trimethyl phosphate to model the reaction of Ada with alkylated DNA, and they concluded that the active nucleophiles in those reactions were dissociated thiolate ligands.[6] A body of synthetic and mechanistic work by Carrano and co-workers,[7] Vahrenkamp and co-workers,[8] and others[9] has revealed that the active nucleophiles in alkylations of neutral zinc(II)−thiolate complexes supported by tripodal co-ligands are the intact zinc−thiolate complexes, rather than free thiolate ions in solution, and that the rates of these reactions are often governed by the basicities of the thiolate ligands. Recently, Carrano and co-workers demonstrated the efficacy of hydrogen bonding in attenuating the nucleophilicity of zinc-bound thiolates,[10] results which may provide insight into the biological mechanism for regioselective S-alkylation of the Cys_4Zn active site in the Ada protein. Alkylations of organo-metallic iron(II)−thiolates have also been examined,[11,12] demonstrating the importance of metal−thiolate orbital energies in governing the reactivity of these complexes.[12]

Our interest in metal−thiolate complexes originates from efforts to model the active-site chemistry of superoxide reductase, a cysteine-ligated non-heme iron enzyme that catalyzes the one-electron reduction of superoxide to hydrogen peroxide in some anaerobes and microaerophiles.[13] Model compounds such as $[L^8py_2Fe(SAr)]^+$ (**1**, Scheme 1) replicate both the square-pyramidal N_4S coordination sphere and the high-spin ferrous electronic ground state of the reduced enzyme.[14] Our work with **1** has led us to prepare and study the nucleophilic reactivity of structurally related cobalt(II)−, nickel(II)−, and zinc(II)−thiolate complexes **2**−**4**. In this article, we demonstrate that these metal(II)−thiolate complexes are alkylated by benzyl bromide according to a common, bimolecular mechanism but with rates that are governed by the identity of the central metal ion. This type of metal ion dependence has not been previously described for alkylations of metal−thiolate complexes that retain their

integrity in solution. Electronic structure calculations performed using density functional theory (DFT) afford a detailed description of the bonding in these metal−thiolate complexes, provide insight regarding the metal ion control of the thiolate alkylation rate, and offer clues as to Nature's selection of zinc(II) to mediate biologically significant alkyl group transfer reactions.

Results and Discussion

Synthesis, Spectroscopy, and Electrochemistry. The synthetic routes to the metal(II)−thiolate complexes are illustrated in Scheme 2. Reaction of the tetradentate ligand 1,5-bis(2-pyridylmethyl)-1,5-diazacyclooctane (L^8py_2)[15] with hydrated metal(II) perchlorate salts and sodium tetraphenylborate in CH_3CN provides precursor complexes $[L^8py_2Co(CH_3CN)]$-$(BPh_4)_2$ (**5**) and $[L^8py_2Ni](BPh_4)_2$ (**6**) as purple and red crystals, respectively. Both of these precursors contain low-spin metal ions as revealed by room-temperature solid-state magnetic susceptibility measurements performed on crystalline samples (Table 1). This magnetic behavior contrasts with that of the iron(II)-containing precursor complex $[L^8py_2Fe(\eta^1\text{-}FBF_3)]BF_4$, which contains a high-spin iron(II) ion.[14] The ^1H NMR spectrum of $[L^8py_2Ni](BPh_4)_2$ in CD_3CN exhibits resonances that are shifted significantly beyond the diamagnetic region, ranging from $+75$ ppm to -38 ppm. While individual resonances have yet to be assigned, it is clear that while $[L^8py_2Ni](BPh_4)_2$ is diamagnetic as a crystalline solid, the complex is paramagnetic when dissolved in coordinating solvents. This spin state change is most likely due to binding of one or two solvent molecules to the vacant axial coordination position(s) of the square-planar cation in $[L^8py_2Ni](BPh_4)_2$ observed in the X-ray crystal structure (vide infra), generating a five- or six-coordinate, $S = 1$ nickel(II) complex in solution.[16]

Preparation of cobalt(II)− and nickel(II)−thiolate complexes is possible either by adding sodium *p*-toluenethiolate to a solution of the appropriate precursor complex in CH_3OH or by using a convenient, one-pot synthesis. In the latter method, the ligand L^8py_2 is combined with the appropriate hydrated metal-(II) perchlorate in a mixture of CH_3OH and CH_3CN. Addition of sodium *p*-toluenethiolate causes immediate color changes indicative of the formation of the metal(II)−thiolate complexes $[L^8py_2M(SAr)]BPh_4$ (M = Co, **2**; M = Ni, **3**), which are precipitated in high yield by the addition of sodium tetraphenylborate. An analogous one-pot synthesis can be used to prepare the colorless zinc(II)−thiolate complex $[L^8py_2Zn(SAr)]$-BPh_4 (**4**). The cobalt(II)− and nickel(II)−thiolate complexes both contain high-spin metal ions in the solid state (Table 1), which contrasts with the electronic ground states of their precursors, while zinc(II)−thiolate complex is diamagnetic. The ^1H NMR spectrum of $[L^8py_2Zn(SAr)]BPh_4$ in CD_3CN contains sharp, well-resolved resonances for all hydrogen atoms of the complex and no signals attributed to free *p*-toluenethiolate, features that remain unchanged over the $20-45$ °C temperature range. These spectra indicate that either the complex remains intact in solution or that a potential dissociative equilibrium between $[L^8py_2Zn(SAr)]BPh_4$ and its $[L^8py_2Zn]^{2+}$ and aryl-thiolate components is too rapid to be detected by NMR.

(6) (a) Wilker, J. J.; Lippard, S. J. *Inorg. Chem.* **1997**, *36*, 969−978. (b) Wilker, J. J.; Wetterhahn, K. E.; Lippard, S. J. *Inorg. Chem.* **1997**, *36*, 2079−2083.
(7) (a) Hammes, B. S.; Carrano, C. J. *Inorg. Chem.* **2001**, *40*, 919−927. (b) Warthen, C. R.; Hammes, B. S.; Carrano, C. J.; Crans, D. C. *J. Biol. Inorg. Chem.* **2001**, *6*, 82−90.
(8) Brand, U.; Rombach, M.; Seebacher, J.; Vahrenkamp, H. *Inorg. Chem.* **2001**, *40*, 6151−6157.
(9) (a) Chiou, S.-J.; Riordan, C. G.; Rheingold, A. L. *Proc. Natl. Acad. Sci. U.S.A.* **2003**, *100*, 3695−3700. (b) Bridgewater, B. M.; Fillebeen, T.; Friesner, R. A.; Parkin, G. *J. Chem. Soc., Dalton Trans.* **2001**, 4494−4496. (c) Chiou, S.-J.; Innocent, J.; Riordan, C. F.; Lam, K. C.; Liable-Sands, L.; Rheingold, A. L. *Inorg. Chem.* **2000**, *39*, 4347−4353. (d) Grapperhaus, C. A.; Tuntulani, T.; Reibenspies, J. H.; Darensbourg, M. Y. *Inorg. Chem.* **1998**, *37*, 4052−4058.
(10) Smith, J. N.; Shirin, Z.; Carrano, C. J. *J. Am. Chem. Soc.* **2003**, *125*, 868−869.
(11) Treichel, P. M.; Schmidt, M. S.; Koehler, S. D. *J. Organomet. Chem.* **1983**, *258*, 209−216.
(12) Ashby, M. T.; Enemark, J. H.; Lichtenberger, D. L. *Inorg. Chem.* **1988**, *27*, 191−197.
(13) (a) Jenney, F. E., Jr.; Verhagen, M. F.; Cui, X.; Adams, M. W. W. *Science* **1999**, *286*, 306−309. (b) Kurtz, D. M.; Coulter, E. D. *J. Biol. Inorg. Chem.* **2002**, *7*, 653−658.
(14) Halfen, J. A.; Moore, H. L.; Fox, D. C. *Inorg. Chem.* **2002**, *41*, 3935−3943.
(15) Halfen, J. A.; Uhan, J. M.; Fox, D. C.; Mehn, M. P.; Que, L., Jr. *Inorg. Chem.* **2000**, *39*, 4913−4920.
(16) We have isolated and structurally characterized several mono- and bis-solvent (CH_3CN, DMSO) adducts of $[L^8py_2Ni]^{2+}$. In all cases, these complexes are purple and contain high-spin metal centers. Full details of the structures and solution behavior of these compounds will be reported elsewhere. Mitchell, M. H.; Halfen, J. A., unpublished results.
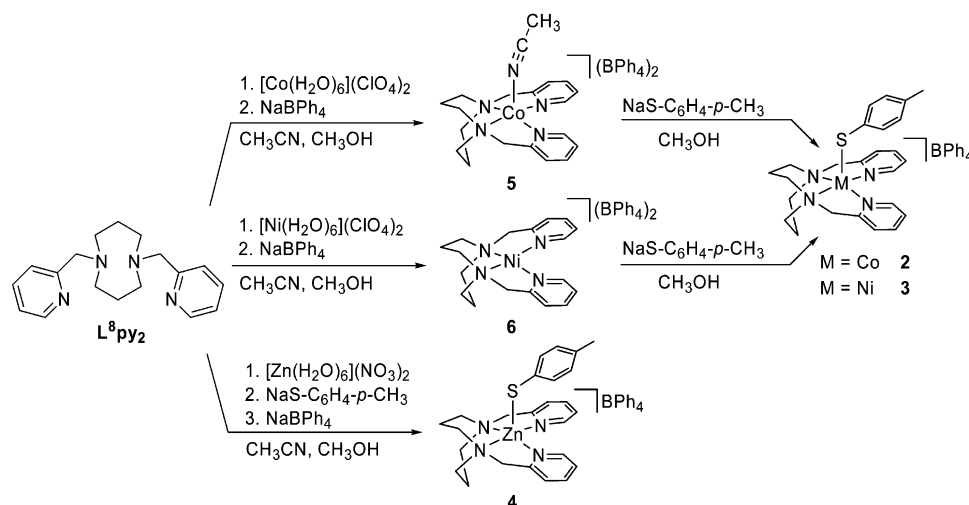
Scheme 2. Synthesis of Complexes **2**–**6**

Table 1. Selected Physical and Spectroscopic Data for **2**, **3**, **5**, and **6**

complex	μ_{eff} $(\mu_B)^a$	λ_{max}, nm $(\epsilon, M^{-1} cm^{-1})^b$	$E^{\circ\prime}$ $(mV)^c$	ΔE_p $(mV)^d$
2	5.0	344 (3300), 378 (2800), sh 430 (1300), 560 (200)	+459 (irr) $(Co^{3+/2+})$	N/A
3	3.7	361 (2100), sh 444 (2500), 474 (2600)	+495 (irr) $(Ni^{3+/2+})$	N/A
			−1315 (Ni^{2+}/Ni^{1+})	130
5	1.9	319 (2100), 491 (140)	−1107 $(Co^{2+/1+})$	75
6	diamag	357 (80), 502 (120)	−765 $(Ni^{2+/1+})$	73

^{a} Solid-state magnetic susceptibility determined at room temperature (diamag = diamagnetic). ^{b} Measured in CH_3CN (sh = shoulder). ^{c} Measured in CH_3CN with 0.1 M Bu_4NClO_4. Potentials are quoted versus SCE at a scan rate of 100 mV/s (irr = irreversible, no cathodic wave observed). ^{d} Difference between anodic and cathodic peak potentials, measured at a scan rate of 100 mV/s (N/A = not applicable). Under the experimental conditions, the ferrocene/ferrocenium couple exhibited ΔE_p ranging from 69 to 80 mV.

Additional evidence against thiolate ligand dissociation from the metal(II)−thiolate complexes was obtained by monitoring the behavior of $[L^8py_2Ni(SAr)]BPh_4$ in the presence of an excess of sodium *p*-toluenethiolate. The ^1H NMR spectrum of the pure complex (in CD_3CN) exhibits two types of signals, including a set of broadened, paramagnetically shifted resonances spanning a chemical shift range of +73 to −15 ppm arising from the $S = 1$ nickel(II)-containing cation. In addition, a distinct set of sharp, unshifted aromatic resonances arising from the diamagnetic BPh_4^- anion ($\delta = 7.29$, 6.95, 6.78 ppm) is apparent within the array of paramagnetic signals. Addition of excess sodium *p*-toluenethiolate to the CD_3CN solution of $[L^8py_2Ni(SAr)]BPh_4$ resulted in the appearance of two new resonances occurring entirely within the diamagnetic region [$\delta = 7.11$ (d, $J = 8$ Hz), 2.28 (s) ppm]. The chemical shifts of these new resonances correspond closely with those of free *p*-toluenethiolate in the absence of the nickel(II) complex ($\delta = 7.12$ (d, $J = 8$ Hz), 6.69 (d, $J = 8$ Hz), 2.13 (s) ppm in CD_3CN; the 6.69 ppm resonance overlaps with a signal from the BPh_4^- anion). The peak widths of the free *p*-toluenethiolate resonances also compare favorably with those of the tetraphenylborate resonances (full width at half-maximum = 12.4 Hz for the 7.11 ppm resonance of the *p*-toluenethiolate ion; fwhm = 16.4 Hz for the 6.95 ppm resonance of the BPh_4^- ion) as well as that of the corresponding aromatic resonance observed in the ^1H NMR spectrum of the pure thiolate (fwhm = 10.4 Hz). If rapid ligand exchange were to occur between $[L^8py_2Ni(SAr)]^+$ and an external thiolate, the ^1H NMR signals of the added thiolate would be broadened significantly and shifted appreciably from their positions in the pure thiolate. However, the sharpness of

the resonances and the lack of substantial changes in chemical shift suggest that the excess *p*-toluenethiolate does not exchange with the bound *p*-toluenethiolate ligand in $[L^8py_2Ni(SAr)]^+$. Taken together, the spectroscopic analyses of $[L^8py_2Ni(SAr)]^+$ and $[L^8py_2Zn(SAr)]^+$ suggest that the metal(II)−thiolate complexes retain their structures in solution and, moreover, that thiolate dissociation must be suppressed to the extent that ligand exchange with an external thiolate cannot be detected by ^1H NMR.

The electronic absorption spectra of the cobalt(II) and nickel(II) complexes are highly sensitive to the presence of thiolate ligation, and they provide a convenient diagnostic method for detecting the metallothiolate complexes in solution and monitoring their reactions. Specifically, the weak visible absorption features of the cobalt(II) and nickel(II) precursors are replaced by intense absorption maxima upon coordination of the axial thiolate ligands in maroon $[L^8py_2Co(SAr)]^+$ and orange $[L^8py_2Ni(SAr)]^+$ (Table 1). The optical spectrum of $[L^8py_2Ni(SAr)]^+$ resembles that of a related nickel(II)−thiolate complex $[(Me_4cyclam)Ni(SPh)]^+$ ($Me_4cyclam$ = 1,4,8,11-tetramethyl-1,4,8,11-tetraazacyclotetradecane), which is also orange because of a strong absorption band with $\lambda_{max} = 470$ nm ($\epsilon = 3000$ M^{-1} cm^{-1}).[17] While detailed spectroscopic analyses have yet to be performed, it is relatively straightforward to assign the intense absorption features of $[L^8py_2Co(SAr)]^+$ and $[L^8py_2Ni(SAr)]^+$ as thiolate-to-metal charge transfer (CT) transitions. These absorption features uniformly shift to lower energy as the central metal ion is changed from Fe to Co to Ni (Figure

(17) Ram, M. S.; Riordan, C. G.; Ostrander, R.; Rheingold, A. L. *Inorg. Chem.* **1995**, *34*, 5884−5892.
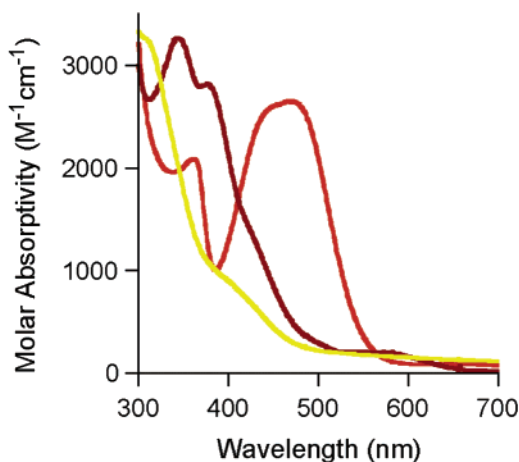
Figure 1. Electronic absorption spectra of **1** (M = Fe; yellow line), **2** (M = Co; brown), and **3** (M = Ni; orange) in CH_3CN.

1), suggesting that the energy gap between the thiolate-based donor orbitals and the metal-based acceptor orbitals decreases within this series. The absence of intense thiolate-to-metal CT transitions for the zinc(II)−thiolate complex correlates with its completely filled d-orbital manifold.

The cyclic voltammograms of the cobalt(II) and nickel(II) precursor compounds each exhibit a single, reversible redox couple, demonstrating that access to the univalent oxidation state is possible for both complexes (Table 1). No oxidative processes are observed for either complex between 0 and 1200 mV (vs SCE). The electrochemical reductions of the precursors occur at a significantly lower potential than the Cu(II)/Cu(I) couple in $[L^8py_2Cu]^{2+}$ ($E^{\circ\prime} = -200$ mV vs Ag/AgCl).[15] The electrochemical behavior of $[L^8py_2Ni]^{2+}$ parallels that of related square-planar Ni(II) complexes bound by either the tetradentate ligand *N*,*N*′-bis-[2-(2′-pyridyl)ethyl]-*N*,*N*′-dimethylethylenediamine ($E^{\circ\prime} = -830$ mV vs SCE)[18] or the macrocyclic ligand Me$_4$cyclam ($E^{\circ\prime} = -780$ mV vs Ag/AgCl).[17] The Ni(II)/Ni(I) couple in $[L^8py_2Ni]^{2+}$ is also similar to that of F_{430M}, the pentamethyl ester of the nickel-containing prosthetic group of methyl coenzyme M reductase, for which $E^{\circ\prime} = -748$ mV.[19] These metal-based redox properties change significantly upon coordination of the axial thiolate ligands. Specifically, while both $[L^8py_2Co(SAr)]^+$ and $[L^8py_2Ni(SAr)]^+$ are irreversibly oxidized, only $[L^8py_2Ni(SAr)]^+$ exhibits a redox couple corresponding to the reduction of its metal(II) center. The redox potential of the Ni^{2+}/Ni^{1+} couple in $[L^8py_2Ni(SAr)]^+$ is more than 0.5 V more negative than the corresponding couple in its precursor, $[L^8py_2Ni]^{2+}$, reflecting the greater difficulty with which an electron is added to the less positively charged nickel(II)−thiolate complex. The irreversibile oxidations of $[L^8py_2Co(SAr)]^+$ and $[L^8py_2Ni(SAr)]^+$ parallel the electrochemical behavior of $[L^8py_2Fe(SAr)]^+$ ($E_{pa} = +615$ mV vs SCE).[14] For that complex, the irreversibility of the electrochemical oxidation was attributed to bimolecular coupling of transient iron(III)−thiolate species, leading to iron(II) and disulfide products.

X-ray Crystallography. The X-ray crystal structure of $[L^8py_2Co(CH_3CN)](BPh_4)_2$ (**5**: Figure 2, top) features a square-pyramidal cobalt(II) ion coordinated by the tetradentate ligand

(18) Kryatov, S. V.; Mohanraj, B. S.; Tarasov, V. V.; Kryatova, O. P.; Rybak-Akimova, E. V.; Nuthakki, B.; Rusling, J. F.; Staples, R. J.; Nazarenko, A. Y. *Inorg. Chem.* **2002**, *41*, 923−930.
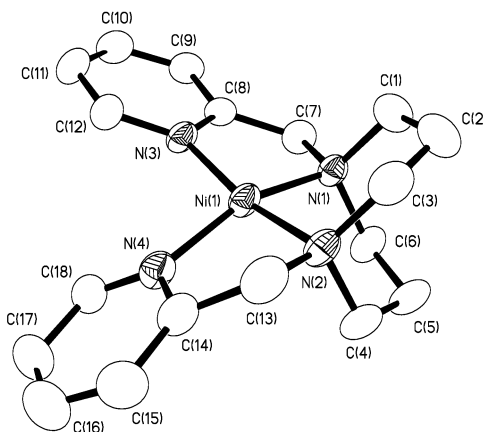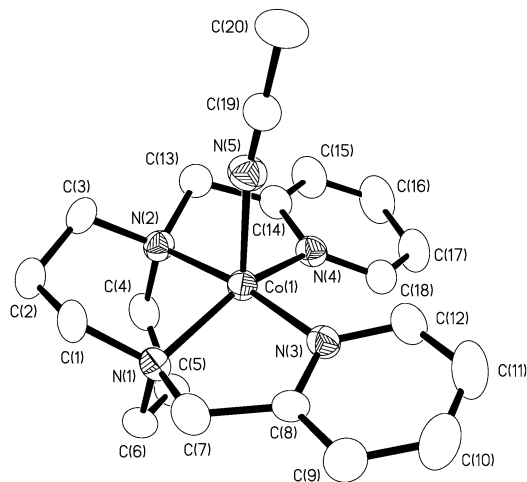(19) Juan, B.; Pfaltz, A. *J. Chem. Soc., Chem. Commun.* **1986**, 1327−1329.

Figure 2. Thermal ellipsoid representations (35% probability boundaries) of the cationic portions of the X-ray crystal structures of **5** (top) and **6** (bottom), with hydrogen atoms omitted for clarity.

L^8py_2 in the metal ion's equatorial plane and a single CH_3CN ligand in an axial position. The cobalt(II) ion is shifted 0.27 Å from the mean plane of the equatorial nitrogen donors toward the axial CH_3CN ligand. The X-ray crystal structure of $[L^8py_2Ni]$-$(BPh_4)_2$ (**6**: Figure 2, bottom) differs from that of **5** in that the central nickel(II) ion in **6** lacks an axial donor and adopts a distorted square-planar geometry. The Ni−N bonds in **6** are uniformly shorter than the Co−N bonds found in **5** (Table 2), reflecting both the reduced ionic radius and the lower coordination number of the nickel(II) ion relative to that of cobalt(II) in these complexes. An acetonitrile molecule is found in the lattice of **6**, although the long Ni···N distance of 2.988(4) Å precludes any significant bonding interactions between the metal ion and the solvate. Comparison of the structure of the cation in **6** to that in $[L^8py_2Cu](ClO_4)_2$ reveals that both metal complexes adopt distorted square-planar geometries and that the equatorial planes of each metal ion are ruffled to similar extents: the average deviation of the nitrogen atoms from the mean equatorial plane in **6** is 0.27 Å, compared to 0.29 Å in the copper(II) complex.[15]

The X-ray crystal structures of metal(II)−thiolate complexes (**2**−**4**: Figure 3) are topologically similar and are highly reminiscent of the structure of the cation in $[L^8py_2Fe(SAr)]^+$.[14] Each of these complexes is characterized by the presence of a pentacoordinate metal ion in a distorted square-pyramidal geometry. Within this series of complexes, the metal−sulfur

Table 2. Significant Interatomic Distances (Å) and Angles (deg) for **2**−**6**

complex	**2** (M = Co)	**3** (M = Ni)	**4** (M = Zn)	**5** (M = Co)	**6** (M = Ni)
M−N1	2.131(3)	2.104(3)	2.172(4)	2.018(3)	1.919(3)
M−N2	2.157(3)	2.079(3)	2.169(4)	2.002(3)	1.915(3)
M−N3	2.112(3)	2.056(3)	2.200(4)	1.972(3)	1.872(3)
M−N4	2.108(3)	2.103(3)	2.122(3)	2.019(3)	1.901(3)
M−S	2.2670(12)	2.3054(11)	2.2925(13)		
M−N5				2.081(3)	
N1−M−N2	83.79(11)	85.91(11)	82.33(14)	88.83(11)	91.16(14)
N1−M−N3	81.17(12)	82.18(12)	76.16(13)	84.17(11)	86.91(14)
N1−M−N4	140.46(12)	149.74(11)	150.94(14)	151.84(11)	159.08(14)
N2−M−N3	156.24(12)	162.13(12)	134.81(13)	172.31(11)	167.51(15)
N2−M−N4	77.20(11)	79.82(11)	79.75(14)	81.29(11)	86.88(15)
N3−M−N4	103.38(12)	104.26(12)	100.92(13)	103.50(12)	99.27(15)
N1−M−S	106.65(9)	101.59(9)	103.05(11)		
N2−M−S	100.17(9)	98.16(8)	116.95(10)		
N3−M−S	101.70(9)	97.25(9)	106.48(10)		
N4−M−S	110.62(10)	106.73(9)	105.47(10)		
C19−S−M	102.25(3)	104.26(13)	99.89(14)		
N1−M−N5				108.37(12)	
N2−M−N5				95.04(12)	
N3−M−N5				90.21(12)	
N4−M−N5				98.77(12)	

bond lengths vary between 2.267(1) Å for $[L^8py_2Co(SAr)]^+$ and 2.323(3) Å for $[L^8py_2Fe(SAr)]^+$, with the metal−sulfur bond lengths for $[L^8py_2Ni(SAr)]^+$ and $[L^8py_2Zn(SAr)]^+$ falling within this range (Table 2). Comparison of the metrical details of $[L^8py_2Co(SAr)]^+$ and $[L^8py_2Ni(SAr)]^+$ to their precursors reveals significant metal−N bond length increases in the metal-(II)−thiolate complexes, consistent with changes in the solid-state spin states of the central metal ions, from low-spin to high-spin, upon coordination of the thiolate ligands. One structural difference between $[L^8py_2Co(SAr)]^+$ and $[L^8py_2Ni(SAr)]^+$ is noteworthy: while the Co−N bonds are longer than the Ni−N bonds, as is expected on the basis of the radii of the two metal ions, the Co−S bond is shorter than the corresponding bond in the nickel(II)−thiolate complex. However, the significance of this ground-state structural difference in governing the nucleophilic reactivity of these complexes is not obvious, as the observed metal−sulfur bond lengths for the family of metal-(II)−thiolate complexes do not correlate with the reactivity of the complexes with electrophiles (vide infra).

Alkylation Reactivity. The nucleophilic reactivity of the metal(II)−thiolate complexes was first noted upon attempted recrystallization of $[L^8py_2Ni(SAr)]BPh_4$ from CH_2Cl_2. In addition to providing orange crystals of the complex, this procedure also generated a small amount of green crystalline material, later identified as $[L^8py_2NiCl]BPh_4$ by X-ray crystallography.[20] Since the only source of halide in this solution was the recrystallization solvent, we surmised that the chloride complex was generated upon reaction of $[L^8py_2Ni(SAr)]^+$ with CH_2Cl_2,[21] a supposition that prompted us to examine the reactivity of the metal(II)−thiolate complexes with other halogenated electrophiles. While many alkylation studies of

metallothiolate complexes have used reactive alkylating agents such as CH_3I or $(CH_3O)_2SO_2$,[6−10] we chose to use a less activated electrophile, benzyl bromide, in subsequent studies.

Preparative scale reactions were conducted by stirring the metal(II)−thiolate complexes with an excess of benzyl bromide in CH_3CN at room temperature (Scheme 3). For the Fe-, Co-, and Ni-containing complexes, this procedure resulted in a dramatic color change of the solution from the original intense colors of the metal(II)−thiolate complexes to nearly colorless (Fe), light blue (Co), or light green (Ni), while the reaction of the zinc(II)−thiolate complex proceeded without perceptible color change or development. Addition of diethyl ether to these solutions caused the deposition of the metal-containing products of the reaction, identified in the case of cobalt(II) and nickel-(II) as the pentacoordinate metal(II)−bromide complexes $[L^8py_2MBr]BPh_4$ (M = Co, Ni), which were characterized by combustion analysis, and in the case of the nickel(II)−bromide complex, by X-ray crystallography.[22] Following precipitation of the metal-containing products, analysis of the supernatant by GC/MS and ^{1}H NMR revealed the presence of benzyl-*p*-tolylsulfide, $PhCH_2SC_6H_4$-*p*-CH_3, as the sole organic product of the reaction. The structure and composition of this material was confirmed by comparing its chromatographic and mass spectroscopic properties to those of an authentic sample, prepared by the reaction of sodium *p*-toluenethiolate with benzyl bromide in CH_3CN. The inability of the thioether product to coordinate to the metal centers is consistent with previous studies that examined the binding of thioethers to $[(Me_4cyclam)Ni]^{2+}$, which demonstrated that while dialkylsulfides bind weakly to the nickel(II) center (K for sulfide binding ∼0.1 M$^{−1}$), aryl sulfides do not coordinate.[17] Carrano and co-workers observed coordination of a thioether product to a zinc center upon alkylation of a zinc(II)−thiolate precursor by including the

(20) X-ray crystallographic data for $[L^8py_2NiCl]BPh_4$, $C_{42}H_{44}BClN_4Ni$ (fw 709.78). Monoclinic, space group $P2_1/c$, with a = 14.713(3) Å, b = 10.063(3) Å, c = 24.526(3) Å, β = 100.37(2)°, V = 3572(1) Å^3, Z = 4, $2\theta_{max}$ = 50.08°, T = 293(2) K. Full-matrix least-squares refinement on F^2 converged with final R1 = 0.0649 and wR2 = 0.1224 for 4117 reflections with $I > 2\sigma(I)$ and 442 variable parameters. The structure of the cation in this complex is consistent with that in the previously reported complex $[L^8py_2NiCl]ClO_4$; Bu, X.-H.; Fang, Y.-Y.; Shang, Z.-L.; Zhang, R.-H.; Zhu, H.-P.; Liu, Q.-T. *Acta Crystallogr.* **1999**, *C55*, 39−41.
(21) For a recent report of a similar reaction of a Ni(II)−thiolate complex with CH_2Cl_2, see: Wang, Q.; Marr, A. C.; Blake, A. J.; Wilson, C.; Schröder, M. *Chem. Commun.* **2003**, 2776−2777.
(22) $[L^8py_2CoBr]BPh_4$: Anal. Calcd for $C_{42}H_{44}BBrCoN_4$: C, 66.86; H, 5.88; N, 7.43. Found: C, 66.76; H, 5.92; N, 7.39. $[L^8py_2NiBr]BPh_4$: Anal. Calcd for $C_{42}H_{44}BBrNiN_4$: C, 66.88; H, 5.88; N, 7.43. Found: C, 66.82; H, 5.88; N, 7.36. X-ray crystallographic data for $[L^8py_2NiBr]BPh_4$, $C_{42}H_{44}BBrN_4$-Ni (fw 754.24): Monoclinic, space group $P2_1/n$, with a = 11.233(2) Å, b = 11.165(2) Å, c = 29.413(6) Å, β = 98.61(3)°, V = 3647(1) Å^3, Z = 4, $2\theta_{max}$ = 49.96°, T = 293(2) K. Full-matrix least-squares refinement on F^2 converged with final R1 = 0.0691 and wR2 = 0.1069 for 4045 reflections with $I > 2\sigma(I)$ and 442 variable parameters.
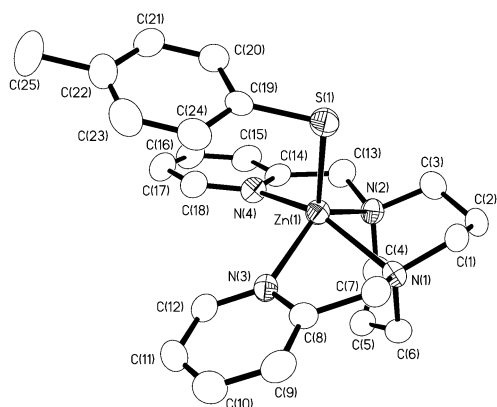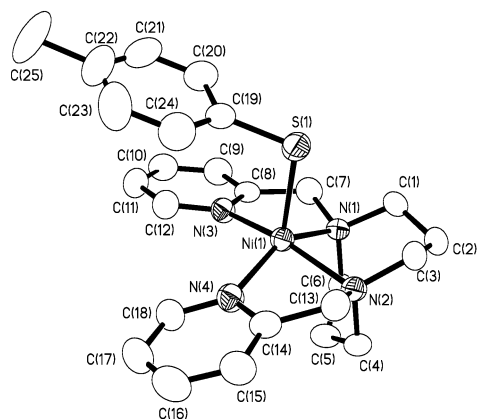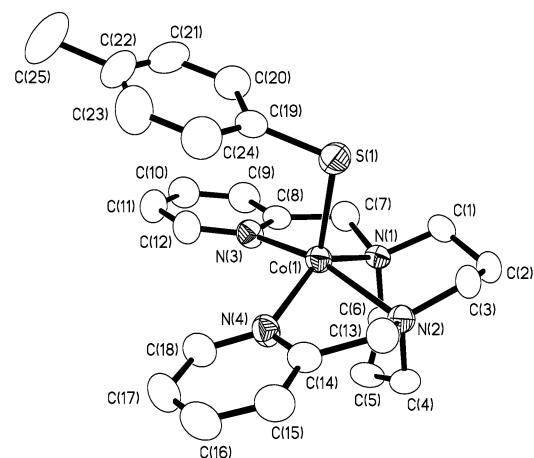
Figure 3. Thermal ellipsoid representations (35% probability boundaries) of the cationic portions of the X-ray crystal structures of **2** (M = Co, top), **3** (M = Ni, middle), and **4** (M = Zn, bottom), with hydrogen atoms omitted for clarity.

Scheme 3. Alkylation of Metal(II)−Thiolate Complexes

Table 3. Second-Order Rate Constants (k_2) for the Reactions of $[L^8Py_2M(SAr)]^+$ with $PhCH_2Br$ at 303(1) K

$[L^8py_2M(SAr)]^+$	k_2, $M^{-1} s^{-1}$
M = Fe	$4.9(3) \times 10^{-3}$
M = Co	$3.1(2) \times 10^{-3}$
M = Ni	$3.0(1) \times 10^{-2}$
M = Zn	$2.9(4) \times 10^{-2}$
NaSAr	$\gg 3 \times 10^{-2}$

Figure 4. Representative first-order kinetics plots for the reactions of **2** (M = Co; upper trace, ◇) and **3** (M = Ni; lower trace, △) with benzyl bromide under pseudo-first-order conditions at 30 °C. Rate constants derived from the slopes of these linear plots and others are provided as Supporting Information (Tables S1−S3).

thiolate/thioether moiety as part of a larger chelating ligand, although the thioether was easily displaced by anionic donors.[7a]

The thiolate alkylation reaction is accompanied by a smooth decay of the UV−visible (M = Fe, Co, Ni) or ^{1}H NMR (Zn) spectroscopic features attributed to the metal(II)−thiolate complexes, with concomitant appearance of features (either electronic absorption bands or ^{1}H NMR resonances) that are characteristic of the metal-containing products of the reactions. Thus, the rates of these reactions were readily determined by monitoring the decay of the spectroscopic features of the complexes as a function of time. Under pseudo-first-order conditions (greater than 10-fold excess of $PhCH_2Br$), the reactions exhibit a first-order dependence on the concentrations
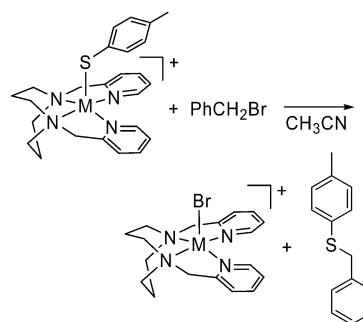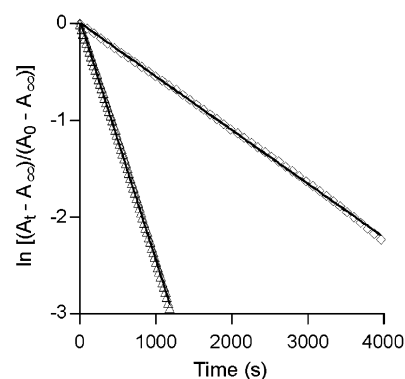
of the metal(II)−thiolate complex. Pseudo-first-order rate constants (k_{obs}; Table S1) were determined using standard first-order plots, which were linear over 3 to 4 half-lives (Figure 4). Varying $[PhCH_2Br]$ while remaining under pseudo-first-order conditions revealed a first-order dependence of k_{obs} on $[PhCH_2Br]$. Thus, the alkylation reaction is an apparent second-order process described by the rate law: rate = $k_2[L^8py_2M(SAr)^+]$-$[PhCH_2Br]$. Of particular significance is the disparity of the second-order rate constants k_2 among these complexes (Table 3): while k_2 for M = Fe(II) and Co(II) is similar, these rate constants are approximately 1 order of magnitude smaller (slower) than k_2 for M = Ni(II) and Zn(II). The enhanced reaction rates for Ni(II) and Zn(II) complexes over the Fe(II) and Co(II) complexes and the divergence of this trend from biological precedent (vide infra) prompted us to further examine the mechanism of this thiolate alkylation reaction. In this case, one representative pair of complexes, the Co(II)− and Ni(II)−thiolate complexes, was chosen because of the ease of monitoring their reactions with benzyl bromide by UV−visible spectroscopy.

Analysis of the temperature dependence of k_2 for these two complexes suggests that the divergent reaction rates are not rooted in a change in the reaction mechanism. Pseudo-first-
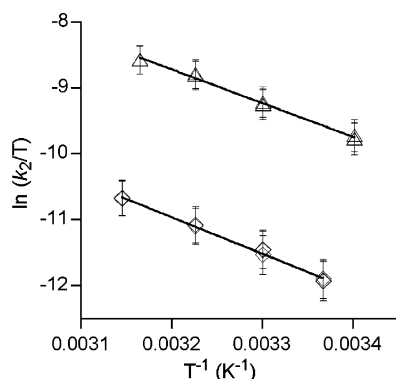
Figure 5. Eyring plots for the reactions of **2** (M = Co; lower trace, ◇) and **3** (M = Ni, upper trace, △) with benzyl bromide. Activation parameters derived from these plots are provided in the text.

order rate constants (k_{obs}) were measured, using a constant [PhCH$_2$Br], for Co(II) and Ni(II) (Table S3); these k_{obs} were converted into second-order rate constant k_2, and an Eyring analysis of the temperature dependence of k_2 yielded activation parameters $\Delta H^{\ddagger}$ and $\Delta S^{\ddagger}$ (Figure 5). The reactions of these two complexes with benzyl bromide exhibit comparable activation parameters (M = Co: $\Delta H^{\ddagger} = 45(2)$ kJ mol^{-1}, $\Delta S^{\ddagger} = -144(6)$ J mol^{-1} K^{-1}; M = Ni: $\Delta H^{\ddagger} = 43(3)$ kJ mol^{-1}, $\Delta S^{\ddagger} = -134(8)$ J mol^{-1} K^{-1}), implicating a common reaction mechanism for both complexes.

Two mechanistic possibilities should be considered to rationalize the available kinetic, thermodynamic, and spectroscopic data for the reactions of the metal(II)−thiolate complexes with benzyl bromide: an S$_N$2-like process, involving rate-limiting nucleophilic attack of the intact metal(II)−thiolate complexes on the electrophile, and an alternative process in which the dissociated thiolate ligands are the active nucleophiles. The clean second-order kinetics spanning a range of temperatures suggest that benzyl bromide reacts with only one nucleophile in solution. If thiolate dissociation were to occur at a rate comparable to alkylation of the metal(II)−thiolate complex, a two-term rate law ($v = k[\text{L}^8\text{py}_2\text{M(SAr)}^+] + k'[\text{L}^8\text{py}_2\text{M(SAr)}^+][\text{PhCH}_2\text{Br}]$), in which the unimolecular term describes the rate of thiolate dissociation and the bimolecular term describes the rate of metallothiolate alkylation, would be necessary to model the observed kinetics. In the limit of slow thiolate dissociation ($k \ll k'$), this two-term rate law collapses to the simple second-order rate law observed for the current set of metal(II)−thiolate complexes. However, because a free thiolate ion is a more potent nucleophile than a cationic metallothiolate complex, the production of even a small concentration of free thiolate ions might contribute significantly to the overall reaction rate. Indeed, NMR experiments designed to measure the rate of alkylation of sodium *p*-toluenethiolate by benzyl bromide in CD$_3$CN revealed that this reaction is significantly faster ($k_2 \gg 3 \times 10^{-2}$ M^{-1} s^{-1}) than the alkylation of the metallothiolate complexes by the same electrophile. Thus, the kinetic behavior of the thiolate alkylation reaction cannot completely eliminate the possibility of thiolate dissociation playing a role in the reactivity of these complexes. Despite this unavoidable ambiguity, spectroscopic studies of the Ni(II)− and Zn(II)−thiolate complexes by ^{1}H NMR (*vide supra*) indicate that the structures of the metal(II)−thiolate complexes are retained in solution and that thiolate exchange (and hence, thiolate ligand dissociation) cannot be detected for even the most reactive nickel(II)−thiolate complex. It was the observation of

rapid ligand exchange by NMR spectroscopy that led Lippard and co-workers to conclude that the active nucleophiles in alkylations of [M(SPh)$_4$]$^{2-}$ (M = Hg, Zn) were dissociated thiolate ions rather than intact metallothiolate complexes.[6] The same study noted that the tendency for thiolate dissociation was directly related to the charges of the metal(II)−thiolate complexes, with dissociation being significant for anionic metallothiolate complexes but largely suppressed for neutral species.[6] Thus, our spectroscopic observations are corroborated by simple electrostatic considerations that also argue against thiolate dissociation, as the loss of an anionic ligand from an already cationic complex would generate an even more positively charged product. Furthermore, the large negative entropies of activation suggest the operation of a mechanism that involves significant ordering in the transition state. On the basis of similar thermodynamic data, Carrano and co-workers[7b] and Riordan and co-workers[9a] proposed that the active nucleophiles in S-methylation reactions of neutral zinc(II)−thiolate complexes were intact complexes, rather than free thiolate ions.

Electronic Structure Calculations. The possible role of the metal ion in determining alkylation reactivity was explored using DFT methods. Spin unrestricted single-point calculations were performed on the high-spin Fe(II), Co(II), and Ni(II) complexes, while spin-restricted calculations were used to study the electronic properties of the free *p*-toluenethiolate ligand and the closed-shell Zn(II) complex. For the single-point calculations, the geometries were based on the corresponding X-ray crystal structures, and in each case the entire complex (minus the counterion) was included in the calculation.

It should be noted that a rigorous assessment of reaction rates requires calculation of transition-state energies, which was not attempted in this study. Instead, our focus is on the ground-state structures and properties of the metal−thiolate complexes. Since the reaction of these complexes with benzyl bromide is strongly product-favored, it is assumed that the transition state occurs quite early along the reaction coordinate. This is consistent with the small $\Delta H^{\ddagger}$ values determined experimentally for the Co(II) and Ni(II) complexes. Thus, the transition-state has primarily reactant character, and differences in alkylation reactivity across the series of metal−thiolate complexes can be inferred from our ground-state calculations.[23]

Bonding Description of Metal(II)-Thiolate Complexes. DFT calculations were performed on the free *p*-toluenethiolate ligand to discern the relevant molecular orbitals (MOs) for thiolate−metal bonding. In agreement with previous studies of aryl thiolates,[24] the two highest-occupied MOs have primarily sulfur 3p-orbital character, although both are delocalized onto the aromatic ring (Figure 6, top). Using previously established nomenclature, we labeled these thiolate π-orbitals according to their orientation with respect to the benzene ring: π_{ip} lies in the plane of the aromatic ring, while π_{op} is perpendicular to this plane.[25] The bonding interactions of the π_{ip} and π_{op} orbitals with the metal d orbitals depend on two structural parameters: the M(II)−S−C^1 bond angle and the M(II)−S−C^1−C^2 dihedral angle.[25] The X-ray crystal structures of [L^{8}py$_2$M(SAr)]$^+$ reveal

(23) Hammond, G. S. *J. Am. Chem. Soc.* **1955**, *77*, 334−338.
(24) (a) McNaughton, R. L.; Tipton, A. A.; Rubie, N. D.; Conry, R. R.; Kirk, M. L. *Inorg. Chem.* **2000**, *39*, 5697−5706. (b) McMaster, J.; Carducci, M. D.; Yang, Y.; Solomon, E. I.; Enemark, J. H. *Inorg. Chem.* **2001**, *40*, 687−702.
(25) Davis, M. I.; Orville, A. M.; Neese, F.; Zaleski, J. M.; Lipscomb, J. D.; Solomon, E. I. *J. Am. Chem. Soc.* **2002**, *124*, 602−614.
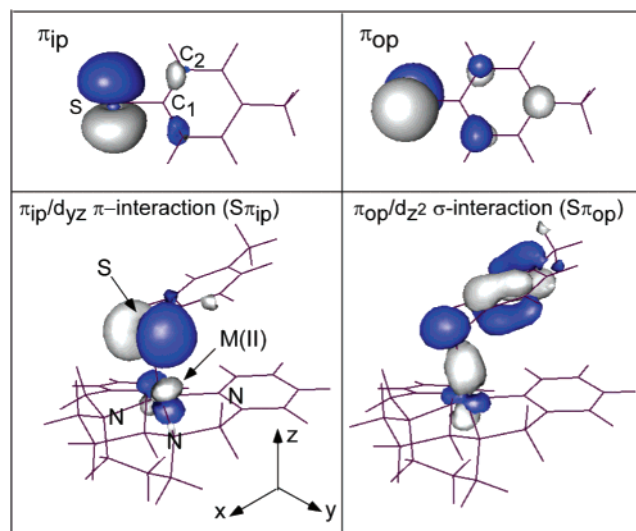
Figure 6. (Top) π_{ip} and π_{op} molecular orbital contour plots of the free *p*-toluenethiolate ligand. (Bottom) Orbital contours depicting the $S\pi_{ip}$ and $S\pi_{op}$ MOs of the Ni(II) complex **3**, illustrating the π- and σ-interactions between the M(II) d-orbitals and π-based ligand orbitals. Similar plots were obtained for the Fe(II) and Co(II) complexes, although for these complexes $S\pi_{ip}$ is π-*bonding* with respect to the metal−thiolate bond.
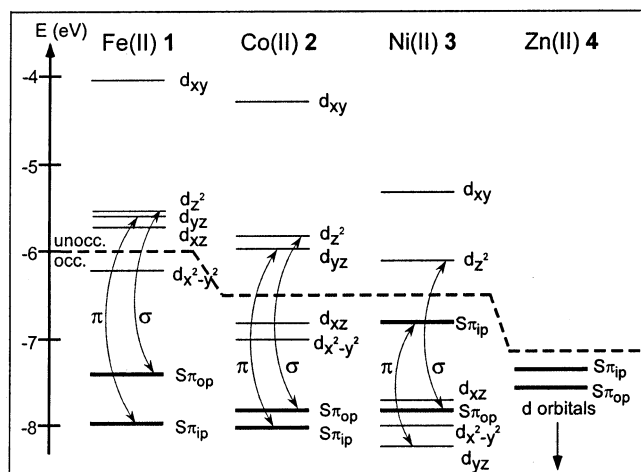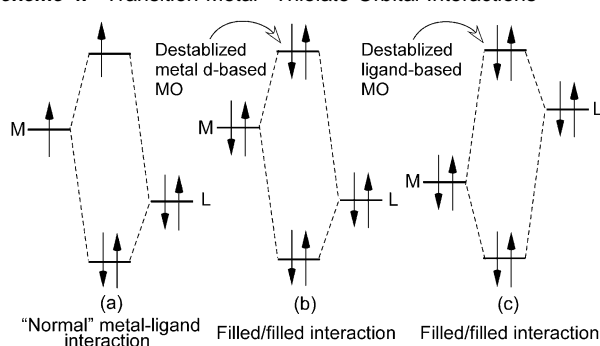

Figure 7. DFT-calculated molecular orbital energy-level diagrams for the metal(II)−thioalte complexes (only the spin-down MOs are shown for the open-shell complexes). The pairs of MOs that result from the dominant metal−thiolate σ- and π-interactions are connected by arrows.

M(II)−S−C angles of 97−104° and dihedral angles between 81° and 111°. Since both sets of angles are near 90°, the π_{op} orbital points primarily along the metal−sulfur bond and forms a σ bond with the metal d_{z^2} orbital. The π_{ip} orbital is largely perpendicular to the M(II)−S bond vector and interacts in a π fashion with the metal d_{yz} orbital (Figure 6, bottom).[28]

Figure 7 depicts the energies of the relevant spin-down MOs for the paramagnetic complexes obtained from spin-unrestricted calculations, as well as the results from the spin-restricted

(26) Caulton, K. G. *New. J. Chem.* **1994**, *18*, 25−41.
(27) (a) Grapperhaus, C. A.; Darensbourg, M. Y. *Acc. Chem. Res.* **1998**, *31*, 451−459. (b) Bellefeuille, J. A.; Grapperhaus, C. A.; Derecskei-Kovacs, A.; Reibenspies, J. H.; Darensbourg, M. Y. *Inorg. Chim. Acta* **2000**, *300*, 73. (c) Grapperhaus, C. A.; Patra, A. K.; Mashuta, M. S. *Inorg. Chem.* **2002**, *41*, 1039−1041. (d) Tyler, L. A.; Noveron, J. C.; Olmstead, M. M.; Mascharak, P. K. *Inorg. Chem.* **1999**, *38*, 616−617.
(28) The coordinate system for complexes **1**−**3** is shown in Figure 6 (bottom). This orientation allows for pure d_{xy} and d_{yz} orbitals, but interchanges the identities of the d_{xy} and $d_{x^2-y^2}$ orbitals.

Scheme 4. Transition Metal−Thiolate Orbital Interactions

calculation for the diamagnetic Zn(II) complex. For complexes with $S > 0$, spin-polarization lowers the energy of the spin-up metal d orbitals, resulting in substantial mixing with the ligand-based orbitals. The nature of metal−thiolate bonding is therefore inferred from the relevant spin-down MOs.

Studies of Fe(II)-bound thiolates using photoelectron spectroscopy indicate that the rate of alkylation correlates with the energies of the thiolate-based MOs.[12] The metal ions modulate the energies of the ligand-based MOs, and thus the identity and oxidation state of the metal strongly influence alkylation reactivity. For divalent metals of the first-row transition series, three electronic effects influence the metal−sulfur bond. First, because of changes in effective nuclear charge, the M(II) d-based MOs decrease in energy relative to the thiolate π-based MOs as one progresses from left to right across the periodic table. As is evident in Figure 7, the spin-down thiolate-based orbitals of the Fe(II) complex lie significantly lower in energy than the metal d-based MOs. The situation is reversed for the Zn(II) complex, in which the highest occupied MOs are thiolate in character and lie well above the metal d-based MOs. Since the extent of metal−ligand bonding is highly dependent on the energy difference between interacting orbitals, the gap between thiolate π-based and metal d orbitals determines metal−thiolate covalency. The DFT calculations correlate nicely with the spectroscopic results presented above, as the decreasing energies of the CT bands from M = Fe → Co → Ni (Figure 1) reflect the diminishing energy gap between the thiolate- and metal-based MOs.

The second effect is associated with the high d-electron count of late transition-metal ions. Overlap between a filled ligand orbital and half-filled metal d orbital results in stabilization of the ligand-based orbital and a net transfer of electron density onto the metal (see Scheme 4, part a). Yet if overlap occurs between two doubly occupied orbitals, the bonding interaction results in no net transfer of electron density from the thiolate to the metal (Scheme 4, part b). Moreover, if the ligand orbital is higher in energy than the filled metal d orbital (Scheme 4, part c), the destabilization of the ligand orbital enhances the nucleophilicity of the complex. Such "filled/filled interactions" or "four-electron repulsions" have been frequently used to justify structure, reactivity, and redox properties for a range of diamagnetic organometallic complexes,[12,26] as well as a smaller number of paramagnetic species.[27c,d]

For the Fe(II) complex (d^6 configuration, $S = 2$), the lone spin-down d electron resides in an MO with predominately Fe $d_{x^2-y^2}$ character (the spin-down HOMO in Figure 7).[28] Consequently, the spin-down thiolate π-based MOs are stabilized through bonding interactions with two half-filled d orbitals, d_{yz}

Table 4. Mulliken Charge and Spin Populations and M(II)/S Covalency Parameters[a] from DFT Calculations

[L⁸py₂M(SAr)]⁺	Mulliken charge		Mulliken spin		M(II)/S covalency[a]	
	M(II)	S	M(II)	S	π_{op}	π_{ip}
M = Fe	0.82	−0.30	3.59	0.23	13	14
M = Co	0.73	−0.27	2.41	0.33	18	19
M = Ni	0.71	−0.30	1.37	0.26	30	32
M = Zn	0.75	−0.35	N/A	N/A	5	4

[a] The M(II)/S covalency parameter is the percent M(II) 3d, 4s, and 4p character in the two-thiolate π-based molecular orbitals. N/A = not applicable.

and d_{z^2}. In the corresponding Co(II) complex (d^7 configuration, $S = 3/2$), the second spin-down electron occupies the d_{xz} orbital that is orthogonal to both thiolate π-orbitals. This results in a situation similar to that found for the Fe(II) complex, although the stabilization of the thiolate orbitals is slightly greater for Co(II) because of the smaller energy gap between interacting orbitals, leading to increased covalency in the Co(II)−S bond.

The bonding scheme of the Ni(II) complex (d^8 configuration, $S = 1$) reflects the fact that the thiolate π-orbitals are almost isoenergetic with the Ni(II) d orbitals. Moreover, both the d_{xz} and d_{yz} orbitals are now doubly occupied, causing the thiolate π_{ip} orbital to experience a filled/filled interaction. On the basis of calculated orbital compositions, this filled/filled interaction produces a destabilized MO that is 62% thiolate π_{ip} in character, while the stabilized MO is mainly (55%) Ni d_{yz}, although considerable metal−thiolate covalency exists. Consequently, unlike the Fe(II) and Co(II) complexes, the Ni(II) complex has a spin-down HOMO that is primarily thiolate-based. Moreover, the Ni(II) π_{ip}-based MO is ~1.2 eV higher in energy than its counterparts in the Fe(II) and Co(II) complexes. Since this MO is one of the key frontier orbitals involved in the alkylation reaction, its destabilization due to filled/filled interactions provides a convincing rationale for the high reactivity of the Ni(II) complex relative to that of the Fe(II) and Co(II) complexes.

The electronic structure of the Zn(II) complex deserves special mention. Unlike the other metal complexes, the thiolate π-orbitals of the Zn(II) complex interact only weakly with the metal d orbitals that are completely filled and lie ~6 eV lower in energy than the sulfur-based HOMO. Consequently, the notion of filled/filled interactions with metal d orbitals is not applicable to this complex. Here, the thiolate-based π-orbitals contain merely 5% zinc character (primarily from unoccupied Zn(II) 4s and 4p orbitals), suggesting a Zn−S bond with dominant ionic character. Systematic changes in the functionals and basis sets used in our calculations did not significantly affect the calculated contributions of zinc orbitals to the thiolate-based MOs. Table 4 shows that the M(II)−thiolate bonds of the Co(II) and Ni(II) complexes are more covalent than that in the Zn(II) complex, as determined by Mulliken charge analysis and orbital composition.

Despite the lack of filled/filled interactions with the zinc d orbitals, the rate data indicate that the Ni(II) complex is just as nucleophilic as the Zn(II) complex. Previous computational studies of zinc−hydroxide and zinc−alkoxide complexes have demonstrated that −OH/OR nucleophilicity is related to both the charge on the oxygen atom and the energy of the oxygen

lone pair.[29] Thus, the strongly ionic character of the Zn−S bond compensates for the absence of filled/filled repulsions, since it increases the charge density on the thiolate sulfur atom (Table 4). Negative charge density on the nucleophilic atom facilitates interaction with the partial positive charge on the electrophile, increasing the rate of reaction.

The third electronic property that changes across the transition-metal series is the overall spin of the complexes. Alkylation reactions are typically viewed in a spin-restricted framework in which the nucleophile possesses a reactive lone pair (or donor orbital) that interacts with the low-energy acceptor orbital of the electrophile. Since the reactions described above proceed with the thiolate bound to the metal site, a considerable amount of spin density is delocalized onto the sulfur; thus, it is not rigorously correct to invoke a thiolate lone pair. Without detailed transition-state calculations, it is difficult to assess the effect of spin on the rates of reaction, although our results suggest that it plays a small role. Mulliken analysis provides estimates of the charge and spin population of each atom in the complex (see Table 4). Since the Co(II)−S bond is more covalent than the Fe(II)−S bond, the sulfur atom in the Co(II) complex possesses considerably more spin density than the sulfur atom in the Fe(II) complex, despite the smaller overall spin for Co(II). Yet the reactivities of the two complexes are quite similar, and no correlation between spin density and reactivity is apparent.

Computational Studies of Metal(II)−Thioether Complexes. The thioethers generated upon reaction of the metal-(II)−thiolate complexes with benzyl bromide do not remain coordinated to the metal center, but instead are displaced by the bromide ion coproduct. This result is not surprising, since examples of metal−thioether complexes generated via alkylation of metal-bound thiolates are somewhat rare (vide supra). Despite the weak donor abilities of thioether ligands, evidence exists that the thioether products of alkyl transfer in the Ada protein and FPT remain coordinated to the metal center.[30,31] In the Ada protein, the methylated cysteine residue is connected to the protein structure, but in FPT the farnesylated peptide is not covalently bound to the active site. In fact, kinetic studies by Casey and co-workers have indicated that the rate-limiting step of the FPT catalytic cycle is release of the thioether product.[32]

Although the thioether-bound analogues of the metal(II)−thiolate complexes are synthetically inaccessible, it is possible to gain insight into the nature of the M(II)−S$_{thioether}$ bond through computational studies of these putative reaction intermediates. Therefore, full DFT geometry optimizations were performed to obtain structures of the hypothetical methylated complexes [L⁸py₂M(MeSAr)]²⁺ (M = Co(II), **2-CH₃**; Ni(II), **3-CH₃**; Zn(II), **4-CH₃**; Ar = −C₆H₄-*p*-CH₃).[33] In the optimized thioether structures, the (H₃)C−S−C¹ angle is ~102° for all three complexes. The new sulfur−carbon σ-bonding interaction

(29) (a) Bertini, I.; Luchinat, C.; Rosi, M.; Sgamellotti, A.; Tarantelli, F. *Inorg. Chem.* **1990**, *29*, 1460−1463. (b) Bräuer, M.; Perez-Lustres, J. L.; Weston, J.; Anders, E. *Inorg. Chem.* **2002**, *41*, 1454−1463. (c) Xia, J.; Shi, Y.; Zhang, Y.; Miao, Q.; Tang, W. *Inorg. Chem.* **2003**, *42*, 70−77.
(30) (a) Ohkubo, T.; Sakashita, H.; Sakuma, T.; Kainosho, M.; Sekiguchi, M.; Morikawa, K. *J. Am. Chem. Soc.* **1994**, *116*, 6035−6036. (b) Myers, L. C.; Cushing, T. D.; Wagner, G.; Verdine, G. L. *Chem. Biol.* **1994**, *1*, 91−97.
(31) (a) Huang, C.; Casey, P. J.; Fierke, C. A. *J. Biol. Chem.* **1997**, *272*, 20−23. (b) Long, S. B.; Casey, P. J.; Besse, L. S. *Nature* **2002**, *419*, 645−650.
(32) Furfine, E. S.; Leban, J. J.; Landavazo, A.; Moomaw, J. F.; Casey, P. J. *Biochemistry* **1995**, *34*, 6857−6862.
(33) Optimized coordinates are provided as Supporting Information.

Table 5. Effect of Thiolate Alkylation on M(II)−S Bond Lengths (All Values in Å)

thiolate–thioether complexes	X-ray crystal structure results	DFT results		Δ^a
	M(II)–S(thiolate)	M(II)–S(thiolate)	M(II)–S(thioether)	
2/2-CH₃ (M = Co)	2.267	2.224	2.453	0.229
3/3-CH₃ (M = Ni)	2.305	2.335	2.420	0.084
4/4-CH₃ (M = Zn)	2.293	2.288	2.506	0.218

[a] Δ = difference in M(II)−S bond lengths for the DFT-optimized geometries of the thiolate and thioether-bound complexes (**X** and **X-CH₃**, respectively).

involves the thiolate π_{ip}-based orbital that, consequently, is no longer available for bonding to the metal center. The remaining thiolate π_{op}-based orbital is oriented primarily along the M(II)−S bond axis to develop a weak σ-bond with the metal d_{z^2} orbital.

To facilitate comparison and test the validity of our computational methods, geometry optimizations were also performed on the metal(II)−thiolate complexes. The optimized structures are in good agreement with the crystallographically determined geometries; i.e., the M(II)−N$_{1,2}$ bond distances increased by 0.05 to 0.12 Å, while all other bond distances changed by <0.05 Å and most angles changed by <5°. Table 5 demonstrates the large effect of alkylation on the M(II)−S bond lengths.[34] Upon alkylation, the zinc−sulfur bond in the DFT-optimized structures is elongated by 0.22 Å. The resulting Zn−S$_{thioether}$ bond distance of 2.51 Å is close to the value of 2.56 Å reported by Carrano and co-workers for a five-coordinate Zn(II)−thioether complex.[7a] Since the zinc−sulfur bond has a large electrostatic component, the loss in ligand charge as the anionic thiolate is converted to the neutral thioether results in substantial weakening of this bond. Analysis of the MOs of the Zn(II)−thioether complex reveals that methylation reduces the energy difference between the sulfur lone pair(s) and the metal d orbitals from 6 to 4.5 eV, but the gap remains too large for significant filled/filled interactions. As with the Zn(II)−thiolate complex, the thioether-based MOs of the Zn(II)−thioether possess very little metal character.

By comparison, the metal−S$_{thioether}$ bonds in the Co(II)− and Ni(II)−thioether complexes are shorter and stronger due to σ-bonding interactions between the sulfur lone pairs and the half-filled metal d_{z^2} orbitals. Yet the Co(II)−S bond lengthens by 0.23 Å upon S-methylation, which is close to the value found for Zn(II), suggesting an equally large reduction in Co(II)−S bond strength upon alkylation. The fact that the Ni(II)−S bond elongates the least among the three pairs is consistent with earlier work by Darensbourg and co-workers on (low-spin) square-planar Ni(II) thiolate/thioether complexes, in which they showed that Ni−S bond lengths change only slightly upon S-alkylation or S-oxygenation.[27a,b] The strength of the Ni(II)−S$_{thioether}$ bond is readily explained by the loss of the π-type filled/filled interaction upon alkylation of the thiolate ligand, which counteracts the diminished σ-donor strength of the thioether. Our computational results suggest that a similar scenario applies to the high-spin Ni(II) species studied here, accounting for the modest increase (0.085 Å) in the Ni(II)−S bond length in the optimized structures.

A Ni(II)-substituted variant of FPT has been shown to possess greater catalytic activity than apoenzyme, although the Ni(II) form is only ~10% as active as the Co(II)-substituted and

Zn(II)-bound WT enzymes.[31] Even though this result appears to contradict the rate data presented above for the metal(II)− thiolate complexes, an explanation for this discrepancy is found in studies by Casey and co-workers, which demonstrate that release of the thioether product is the rate-limiting step in the FPT mechanism.[32] Since our results indicate that thioethers are expected to bind more tightly to Ni(II) than to Co(II) or Zn(II), the reduced catalytic rate of the Ni(II) form of FPT may arise from slower release of the thioether product, rather than slower thiolate alkylation.

Conclusion

A series of new square-pyramidal metal(II)−thiolate complexes have been synthesized and structurally characterized. These complexes react with benzyl bromide according to a common, bimolecular mechanism with rates that depend on the identity of the central metal ion, a dependence that has been explored using density functional theory calculations. These calculations have revealed that the enhanced nucleophilicity of the nickel(II)− and zinc(II)−thiolate complexes is rooted in either a four-electron, filled/filled orbital repulsion (for the nickel(II)−thiolate complex) or a highly ionic metal(II)−thiolate interaction resulting in enhanced negative charge density on the thiolate sulfur (for the zinc(II)−thiolate complex). While often invoked to rationalize the reactivity of closed-shell organometallic species, we believe that these results represent the first application of the filled/filled orbital repulsion concept to explain reactivity trends of paramagnetic complexes. Although thiolate alkylation occurs at comparable rates for the nickel(II) and zinc(II) complexes, DFT calculations demonstrate that binding of the product thioether is stronger to nickel(II) than to zinc(II) or cobalt(II). These combined results suggest that while nickel(II) may be a functionally competent replacement for zinc(II) in group transfer enzymes, the activity of such metal-substituted variants may be limited by slow release of the thioether product from the nickel(II) center. Indeed, zinc(II) appears to be ideally suited for mediating biological thiolate alkylations, as it provides for a reactive thiolate through an ionic metal−sulfur interaction, as well as for facile product release due to the weakness of the nascent zinc(II)−thioether bond.

Experimental Section

Materials and Methods. Reagents were obtained from commercial sources and used as received unless noted otherwise. Solvents were purified according to standard methods. The tetradentate ligand 1,5-bis(2-pyridylmethyl)-1,5-diazacyclooctane (L⁸py₂) was prepared as described previously.[15] All reactions were conducted, and products were handled under an inert atmosphere using standard Schlenk techniques or in a Vacuum Atmospheres inert atmosphere glovebox. NMR spectra were obtained using a JEOL Eclipse 400 spectrometer. ¹H NMR chemical shifts are reported vs TMS and are referenced to residual solvent peaks. Electronic absorption spectra were measured using a

(34) The L⁸py₂ ligand and its coordination to the M(II) centers is largely unaffected by conversion of the axial ligand from thiolate to thioether. The only significant change is a slight contraction (<0.08 Å) of some of the M(II)−N bonds upon methylation.

Hewlett-Packard 8453 spectrophotometer (190–1100 nm range). Electrochemical experiments were conducted with a BAS Epsilon potentiostat, using a platinum disk working electrode, a silver wire pseudo-reference electrode, and a platinum wire auxiliary electrode. Cyclic voltammograms were obtained in CH_3CN (0.1 M n-Bu$_4$NClO$_4$) with an analyte concentration of 1 mM. Ferrocene was used as an internal standard, and its redox potential under the experimental conditions was scaled to the literature value (+380 mV vs SCE) and other analyte redox potentials scaled accordingly.[35] Elemental analyses were performed by Atlantic Microlabs (Norcross, GA).

[L^{8}py$_2$Co(CH$_3$CN)](BPh$_4$)$_2$ (5). To a solution of L^{8}py$_2$ (0.0532 g, 0.179 mmol) in CH_3CN (3 mL) was added [Co(H$_2$O)$_6$](ClO$_4$)$_2$ (0.0632 g, 0.173 mmol) as a solid, generating a purple-maroon solution. After being stirred for several minutes, a solution of NaBPh$_4$ (0.352 g, 1.03 mmol) in CH_3OH (3 mL) was added, which caused the immediate deposition of a light purple microcrystalline precipitate. This solid was collected by vacuum filtration, washed with copious amounts of CH_3OH and then Et$_2$O, and dried under vacuum: 0.147 g (83%). Recrystallization from hot CH_3CN provided solvated burgundy crystals of **5·CH$_3$CN** suitable for X-ray crystallography. Anal. Calcd for **5·CH$_3$CN**, C$_{70}$H$_{70}$B$_2$CoN$_6$: C, 78.14; H, 6.56; N, 7.81. Found: C, 77.97; H, 6.48; N, 7.68.

[L^{8}py$_2$Ni](BPh$_4$)$_2$ (6). To a solution of L^{8}py$_2$ (0.0556 g, 0.188 mmol) in CH_3CN (3 mL) was added [Ni(H$_2$O)$_6$](ClO$_4$)$_2$ (0.0668 g, 0.183 mmol) as a solid, generating a red solution. After being stirred for several minutes, a solution of NaBPh$_4$ (0.320 g, 0.935 mmol) in CH_3OH (3 mL) was added, which caused the immediate deposition of a red microcrystalline precipitate. This solid was collected by vacuum filtration, washed with copious amounts of CH_3OH and then Et$_2$O, and dried under vacuum: 0.158 g (88%). Recrystallization from CH_3CN/ Et$_2$O provided solvated red crystals of **6·CH$_3$CN** suitable for X-ray crystallography. Anal. Calcd for **6·CH$_3$CN**, C$_{68}$H$_{67}$B$_2$N$_5$Ni: C, 78.90; H, 6.52; N, 6.77. Found: C, 78.51; H, 6.44; N, 6.61.

[L^{8}py$_2$Co(S-C$_6$H$_4$-p-CH$_3$)]BPh$_4$ (2). To a solution of L^{8}py$_2$ (0.0546 g, 0.184 mmol) in CH_3OH (3 mL) was added [Co(H$_2$O)$_6$](ClO$_4$)$_2$ (0.0684 g, 0.186 mmol) as a solid, generating a purple-maroon solution. After being stirred for several minutes, sodium p-toluenethiolate (0.0492 g, 0.337 mmol) was added, followed by a solution of NaBPh$_4$ (0.584 g, 1.71 mmol) in CH_3OH (3 mL), which caused the immediate deposition of a green-brown microcrystalline precipitate. This solid was collected by vacuum filtration, washed with CH_3OH and Et$_2$O, and dried under vacuum: 0.115 g (78%). Recrystallization from DMF/Et$_2$O provided maroon crystals of **2** suitable for X-ray crystallography. Anal. Calcd for **2**, C$_{49}$H$_{51}$BCoN$_4$S: C, 73.77; H, 6.44; N, 7.02. Found: C, 73.49; H, 6.43; N, 7.12.

[L^{8}py$_2$Ni(S-C$_6$H$_4$-p-CH$_3$)]BPh$_4$ (3). To a solution of L^{8}py$_2$ (0.0555 g, 0.187 mmol) in CH_3OH (3 mL) was added [Ni(H$_2$O)$_6$](ClO$_4$)$_2$ (0.0679 g, 0.186 mmol) as a solid. A red solid, [L^{8}py$_2$Ni](ClO$_4$)$_2$, precipitated rapidly, and CH_3CN (2 mL) was added to redissolve this material. After being stirred for several minutes, sodium p-toluenethiolate (0.0486 g, 0.332 mmol) was added, followed by a solution of NaBPh$_4$ (0.282 g, 0.824 mmol) in CH_3OH (3 mL), which caused the immediate deposition of an orange-brown microcrystalline precipitate. This solid was collected by vacuum filtration, washed with CH_3OH and Et$_2$O, and dried under vacuum: 0.126 g (85%). Recrystallization from DMF/Et$_2$O provided orange crystals of **3** suitable for X-ray crystallography. Anal. Calcd for **3**, C$_{49}$H$_{51}$BN$_4$NiS: C, 73.79; H, 6.45; N, 7.02. Found: C, 73.49; H, 6.42; N, 6.96.

[L^{8}py$_2$Zn(S-C$_6$H$_4$-p-CH$_3$)]BPh$_4$ (4). To a solution of L^{8}py$_2$ (0.0768 g, 0.259 mmol) in CH_3CN (3 mL) was added [Zn(H$_2$O)$_6$](NO$_3$)$_2$ (0.0771 g, 0.259 mmol) as a solid. After being stirred for several minutes, sodium p-toluenethiolate (0.0769 g, 0.526 mmol) was added, followed by a solution of NaBPh$_4$ (0.440 g, 1.29 mmol) in CH_3OH (3 mL), which caused the immediate deposition of a colorless microcrystalline

precipitate. This solid was collected by vacuum filtration, washed with CH_3OH and Et$_2$O, and dried under vacuum: 0.154 g (76%). Recrystallization from DMF/Et$_2$O provided colorless crystals of **4** suitable for X-ray crystallography. ^{1}H NMR (400 MHz, CD$_3$CN): δ 8.51 (d, 2H), 8.03 (dt, 2H), 7.51–7.46 (m, 4H), 7.26 (m, 8H), 6.98 (t, 8H), 6.83 (t, 4H), 6.68 (d, 2H), 6.58 (d, 2H), 4.03 (d, 2H), 3.78 (d, 2H), 3.40 (dt, 2H), 3.08–2.96 (m, 4H), 2.59 (t, 1H), 2.55 (t, 1H), 2.37–2.27 (m, 2H), 2.11 (s, 3H), 1.47 (q, 2H) ppm. Anal. Calcd for **4**, C$_{49}$H$_{51}$BN$_4$SZn: C, 73.18; H, 6.39; N, 6.97. Found: C, 73.06; H, 6.31; N, 7.03.

X-ray Crystallography. Single crystals were mounted in thin-walled glass capillaries and transferred to a Bruker-Nonius MACH3S X-ray diffractometer for data collections at 25 °C using graphite monochromated Mo Kα ($\lambda = 0.71073$ Å) radiation. Unit cell constants were determined from a least-squares refinement of the setting angles of 25 intense, high-angle reflections. Intensity data were collected using the $\omega/2\theta$ scan technique to a maximum 2θ value of 50–52°. Absorption corrections were applied on the basis of azimuthal scans of several reflections for each sample. The data were corrected for Lorentz and polarization effects and converted to structure factors using the teXsan for Windows crystallographic software package.[36] Space groups were determined on the basis of systematic absences and intensity statistics. Successful direct-methods solutions were calculated for each compound using the SHELXTL suite of programs.[37] Any non-hydrogen atoms not identified from the initial E-map were located after several cycles of structure expansion and full matrix least-squares refinement on F^2. Hydrogen atoms were added geometrically. All non-hydrogen atoms were refined with anisotropic displacement parameters, while hydrogen atoms were refined using a riding model with group isotropic displacement parameters. Relevant crystallographic information for the compounds is summarized in Table 6. Complete crystallographic data for each compound are provided as Supporting Information in CIF format.

Reaction Rate Measurements. For the reactions of **1**, **2**, and **3** with benzyl bromide, rates were measured by UV–visible spectroscopy by monitoring the decay of the intense UV–visible charge-transfer bands of these complexes as a function of time. Solutions of the complexes were prepared in CH_3CN in volumetric flasks, and then the required amount of benzyl bromide was added by microliter syringe. Additional CH_3CN was added to give final solution volumes of 5.00 mL, yielding metal complex concentrations of 0.5 mM and benzyl bromide concentrations ranging from 43 to 244 mM. After mixing thoroughly, a portion of the solution was transferred to a quartz cuvette and placed in a thermostated cell compartment in a UV–visible spectrophotometer. Complete spectra were recorded throughout the reaction. Pseudo-first-order rate constants (k_{obs}) were calculated from the slopes of standard first-order plots of $\ln[(A_t - A_\infty)/(A_0 - A_\infty)]$ versus time, which were linear over 3 to 4 half-lives (where A is the absorbance at λ_{max} for each complex). Pseudo-first-order rate constants are provided as Supporting Information in Table S1. Second-order rate constants k_2 were determined using the relationship $k_{obs} = k_2[\text{PhCH}_2\text{Br}]$ and are presented in Table 4. Variable temperature pseudo-first-order rate constants for the reactions of **2** and **3** are provided in Table S3.

For the reactions of **4** with benzyl bromide, rates were measured by ^{1}H NMR spectroscopy by monitoring the decay of ^{1}H NMR resonances ascribed to **4** as a function of time. Solutions of the complex in CD$_3$CN were prepared in volumetric flasks, a portion of 4,4′-dimethoxybenzophenone was added as an internal standard, and then the required amount of benzyl bromide was added by microliter syringe. Additional CD$_3$CN was added to give final solution volumes of 1.00 mL, yielding metal complex concentrations of 5.0 mM, internal standard concentrations of 7.0 mM, and benzyl bromide concentrations of 86 mM. After being mixed thoroughly, the entire solution was transferred

(35) Connelly, N. G.; Geiger, W. E. *Chem. Rev.* **1996**, *96*, 877–910.

(36) *TeXsan for Windows*, version 1.02; Molecular Structure Corporation, Inc.: The Woodlands, TX, 1997.
(37) *SHELXTL*, version 6.12 for Windows; Bruker AXS: Madison, WI, 2001.

Table 6. X-ray Crystallographic Data for **2−6**[a]

complex	2	3	4	5·CH₃CN	6·CH₃CN
empirical formula	$C_{49}H_{51}BCoN_4S$	$C_{49}H_{51}BNiN_4S$	$C_{49}H_{51}BN_4SZn$	$C_{70}H_{70}B_2CoN_6$	$C_{68}H_{67}B_2N_5Ni$
fw	797.74	797.52	804.18	1075.78	1034.60
cryst syst	monoclinic	monoclinic	orthorhombic	orthorhombic	triclinic
space group	$P2_1/c$	$P2_1/c$	$P2_12_12_1$	$Pbca$	$P\bar{1}$
a (Å)	10.905(1)	10.860(1)	14.362(1)	18.620(2)	11.355(2)
b (Å)	18.917(2)	18.999(1)	14.835(1)	17.399(2)	13.064(2)
c (Å)	20.445(1)	20.344(2)	19.622(1)	36.260(6)	18.833(2)
α (deg)					88.52(2)
β (deg)	90.99(2)	91.16(1)			86.13(1)
γ (deg)					88.74(2)
V (Å³)	4217.0(6)	4196.7(6)	4180.7(5)	11747(3)	2711.9(7)
Z	4	4	4	8	2
d_{calcd} (Mg m⁻³)	1.257	1.262	1.278	1.217	1.267
cryst size (mm³)	0.46 × 0.40 × 0.25	0.52 × 0.40 × 0.38	0.48 × 0.35 × 0.30	0.42 × 0.40 × 0.28	0.42 × 0.35 × 0.15
abs coeff (mm⁻¹)	0.495	0.551	0.677	0.340	0.406
2θ max (deg)	50.10	50.06	50.02	49.94	51.38
transm range	1.0−0.9278	1.0−0.9572	1.0−0.9487	1.0−0.9168	1.0−0.9275
No. of reflns collected	7432	7808	7940	10268	10393
No. of independent reflns	7432	7391	7335	10268	9851
No. of obsd reflns	4855	4911	4911	5540	6175
No. of variables	505	505	505	714	696
R1 (wR2)[b] $[I > 2\sigma(I)]$	0.0602 (0.1054)	0.0588 (0.0941)	0.0487 (0.0777)	0.0519 (0.1142)	0.0728 (0.1132)
GOF (F^2)	1.028	1.039	1.014	1.010	1.037
difference peaks (e⁻ Å⁻³)	0.240, −0.271	0.233, −0.263	0.232, −0.253	0.326, −0.397	0.219, −0.255

[a] See Experimental Section for additional data collection, reduction, and structure solution and refinement details. [b] R1 = $\sum||F_o| - |F_c||/\sum|F_o|$; wR2 = $\{\sum[w(F_o^2 - F_c^2)^2]\}^{1/2}$ where $w = 1/\sigma^2(F_o^2) + (aP)^2 + bP$.

to an NMR sample tube, and the tube was placed in a thermostated probe of an NMR spectrometer. Complete ¹H NMR spectra were recorded every 300 s for a total of 3−6 h. The ratio of the integrated intensities of the resonances from **4** to the integrated intensities of the methoxy resonance from the internal standard in each spectrum provided a measurement of the concentration of **4**, [**4**], in each spectrum. Pseudo-first-order rate constants (k_{obs}) were determined from the slopes of first-order plots, $\ln[([\mathbf{4}]_t - [\mathbf{4}]_\infty)/([\mathbf{4}]_0 - [\mathbf{4}]_\infty)]$ versus time. Pseudo-first-order rate constants are provided as Supporting Information in Table S2. Second-order rate constants k_2 were determined using the relationship $k_{obs} = k_2[\text{PhCH}_2\text{Br}]$, and the values are presented in Table 3.

Electronic Structure Calculations. Single-point DFT calculations were performed on complexes **1−4** using the ORCA 2.0 software package developed by F. Neese. Spin-unrestricted calculations were performed on **1−3** while spin-restricted calculations were used to study **4**. Computational models were generated on the basis of the corresponding X-ray crystal structures, and in each case the entire complex (minus the counterion) was included in the calculation. Ahlrich's valence triple-ζ basis set[38] with one set of polarization functions[39] on all atoms (including hydrogens) was used, along with the corresponding auxiliary basis set (VTZ_J).[40] The calculations were performed with the local density approximation of Perdew and Wang[41] and the corrections of Becke[42] and Perdew,[43] with an integration grid of 4.0. The gOpenMol program developed by Laaksonen[44,45] was used to generate boundary surface plots of molecular orbitals using an isodensity value of 0.05 b⁻³.

Geometry optimizations were performed with the Amsterdam Density Functional (ADF) 2002.03 software package.[46] These computa-

tions were carried out on a home-built cluster of 20 Intel Xeon processors using ADF basis set IV (triple-ζ with single polarization on the ligand atoms), an integration constant of 4.0, and the Vosko−Wilk−Nusair[47] local density approximation with the nonlocal gradient corrections of Becke[42] and Perdew.[43] Core orbitals were frozen through 1s (O, N,C) and 2p (S, Co, Ni, Zn). Spin-unrestricted optimizations were performed for Co and Ni complexes (**2**, **2-CH₃**, **3**, **3-CH₃**), while spin-restricted optimizations were performed for Zn complexes (**4**, **4-CH₃**). The entire complexes (minus the counterions) were included in the calculations, and all coordinates were optimized.

Supporting Information Available: Tables of k_{obs} for the reactions of **1−4** with benzyl bromide (Tables S1 and S2). Table of k_{obs} for the reactions of **2** and **3** with benzyl bromide as a function of temperature (Table S3). Table of Cartesian coordinates for all DFT geometry-optimized models discussed in the text (Table S4). Cyclic voltammograms for **2**, **3**, **5**, and **6** (Figures S1−S4) (PDF). Complete crystallographic data for **2−6** (CIF). This material is available free of charge via the Internet at http://pubs.acs.org.

JA039419Q

(38) Schaefer, A.; Horn, H.; Ahlrichs, R. *J. Chem. Phys.* **1992**, *97*, 2571.
(39) Ahlrichs, R. Unpublished results.
(40) (a) Eichkorn, K.; Treutler, O.; Ohm, H.; Haser, M.; Ahlrichs, R. *Chem. Phys. Lett.* **1995**, *240*, 283. (b) Eichkorn, K.; Weigend, F.; Treutler, O.; Ahlrichs, R. *Theor. Chem. Acc.* **1997**, *97*, 119.
(41) Perdew, J. P.; Wang, Y. *Phys. Rev. B* **1992**, *45*, 13244−13249.
(42) Becke, A. D. *J. Chem. Phys.* **1986**, *84*, 4524−4529.
(43) Perdew, J. P. *Phys. Rev. B* **1986**, *33*, 8822−8824.
(44) Laaksonen, L. *J. Mol. Graphics* **1992**, *10*, 33.
(45) Bergman, D. L.; Laaksonen, L.; Laaksonen, A. *J. Mol. Graphics Modell.* **1997**, *15*, 301.
(46) (a) Baerends, E. J.; Ellis, D. E.; Ros, P. *Chem. Phys.* **1973**, *2*, 41. (b) Versluis, L.; Ziegler, T. *J. Chem. Phys.* **1988**, *88*, 322−328. (c) te Velde, G.; Baerends, E. J. *J. Comput. Phys.* **1992**, *99*, 84−98. (d) Guerra, C. F.; Snijders, J. G.; te Velde, G.; Baerends, E. J. *Theor. Chem. Acc.* **1998**, *99*, 391−403.
(47) Vosko, S. H.; Wilk, L.; Nusair, M. *Can. J. Phys.* **1980**, *58*, 1200.